

Parity-controlled gate in a two-dimensional neutral-atom array

F. Q. Guo,¹ Shi-Lei Su,^{2,3,*} Weibin Li,^{4,†} and X. Q. Shao^{1,5,‡}

¹Center for Quantum Sciences and School of Physics, Northeast Normal University, Changchun 130024, China

²School of Physics, Key Laboratory of Materials Physics of Ministry of Education, and International Laboratory for Quantum Functional Materials of Henan, Zhengzhou University, Zhengzhou 450001, China

³Institute of Quantum Materials and Physics, Henan Academy of Science, Henan 450046, China

⁴School of Physics and Astronomy, and Centre for the Mathematics and Theoretical Physics of Quantum Non-equilibrium Systems, The University of Nottingham, Nottingham NG7 2RD, United Kingdom

⁵Center for Advanced Optoelectronic Functional Materials Research, and Key Laboratory for UV Light-Emitting Materials and Technology of Ministry of Education, Northeast Normal University, Changchun 130024, China

We propose a parity-controlled gate within a two-dimensional Rydberg atom array, enabling efficient discrimination between even and odd parities of virtually excited control atoms by monitoring the dynamic evolution of an auxiliary atom. This is achieved through the use of spin-exchange dipolar interactions between Rydberg states and coupling between ground states and Rydberg states. For practical applications, we explore its implementation in three-qubit repetition codes and rotated surface codes featuring $XZZX$ stabilizers, enabling single-shot readout of stabilizer measurements. Comprehensive numerical simulations are conducted to assess the feasibility of the proposed approach, taking into account potential experimental imperfections such as unwanted interactions between Rydberg states, atomic position fluctuations, laser phase noise, and Rabi amplitude noise. Our study highlights the inherent advantages of the physical mechanisms underlying parity measurement, demonstrating its reliability and practicality. These findings establish our protocol as a highly promising solution for quantum error detection and computation within Rydberg atom systems, with significant potential for future experimental realizations.

I. INTRODUCTION

Parity measurement plays a pivotal role in various quantum information processing tasks, such as entanglement generation and analysis [1–5], quantum error correction (QEC) [6–9], and quantum algorithms [10–13]. Traditional parity measurement is often implemented through sequential controlled- Z (CZ) or controlled-NOT (CNOT) gates [14–16]. Alternatively, direct construction of multiqubit parity gates provides a more efficient approach [11, 17–22]. Compared to sequential gate methods, parity gates offer the advantage of being locally equivalent to consecutive CZ or CNOT gates that share a common control or target qubit [22]. This design significantly simplifies system calibration by reducing it to a single gate or a minimal number of gates per parity check [20]. Such parity gates are particularly suitable for applications in logical encoding and parity-check syndrome measurements in QEC [23–26], as they are integral to surface codes [16, 20, 21, 27–30]. These codes are implemented in two-dimensional networks of entangled physical qubits and function as stabilizer codes [31]. In this framework, errors are detected by evaluating the parity of four adjacent qubits, typically through measurements of stabilizer operators represented as $ZZZZ$ and $XXXX$, where Z and X denote Pauli operations. The eigenvalues ± 1 of the N -qubit parity operator $\bigotimes_i^N Z_i$ (or $\bigotimes_i^N X_i$) correspond to even and odd parities, respectively [21]. Therefore, parity assessment is a crucial component of quantum error detection.

Rydberg atoms are highly promising candidates for quantum computing and quantum information processing. Their remarkable characteristics, such as long coherence times, the ability to scale up, and significant electric dipole moments [32–38], highlight their potential in a range of applications, including quantum gate implementation [39–51], entanglement preparation [41, 52–60], and quantum simulation [34, 35, 61–72] using techniques such as Rydberg blockade [73, 74], Rydberg antiblockade [75], and Rydberg dressing [76, 77]. Significant progress is being made in the rapid development of one- and two-dimensional arrays featuring individually manipulated Rydberg atoms. These atoms are precisely controlled within optical tweezers [34, 35, 78–81], providing a crucial physical platform to realize fault-tolerant quantum computing in neutral atom systems. Refs. [48, 82–92] have delved into error correction in Rydberg atoms through various encoding methods, with efficient parity measurements emerging as a central focus.

Recently, a nondestructive Rydberg parity measurement, termed a “parity meter,” based on Rydberg antiblockade, has been proposed in Ref. [18], requiring three operational procedures. However, this method is subject to significant variations in atomic spacing, since the scheme becomes inoperative even with a small deviation of less than 1% in the necessary van der Waals (vdW) interaction. In response, Ref. [19] enhances the resilience of the Rydberg parity meter against fluctuations in interatomic distance by employing the unconventional Rydberg pumping mechanism (URP) [93]. However, this adaptation does not reduce the number of operations required to implement the scheme. Sequential or step-by-step procedures have the capacity to enhance vulnerability to errors and decoherence, potentially resulting in a reduction in the efficiency of quantum information processing [39, 94, 95].

* slsu@zzu.edu.cn

† weibin.li@nottingham.ac.uk

‡ shaoxq644@nenu.edu.cn

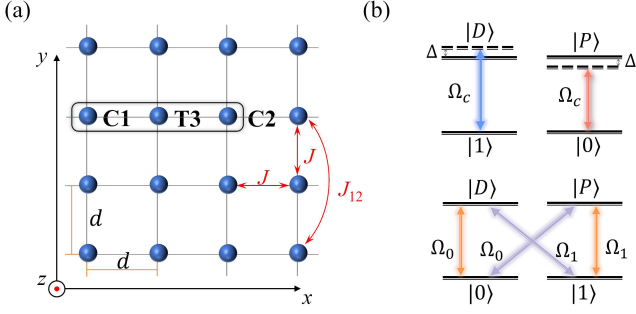


FIG. 1. Atoms are arranged in a square lattice (a) with the spacing d between two adjacent atoms. The dipole-dipole interaction strengths are set as $J_{13} = J_{23} = J$ between the atoms **C1**, **C2**, and **T3**. A laser driving scheme for control atoms (**C1**, **C2**, upper panel) and target atom (**T3**, lower panel) is shown in (b).

In this work, we present a parity-controlled quantum gate tailored for neutral-atom systems. This gate leverages the dipole-dipole interaction within highly excited Rydberg states. The operation is governed by the parity of the control atoms' ground state space: different parities will either preserve the target atom's state or flip it. This design enables parity measurement of two atoms in a single operational step, eliminating the need for multiple sequential actions. To ensure that the parity of the two control atoms remains undisturbed during the process, we apply two off-resonant lasers to induce virtual excitations to Rydberg states. Additionally, we utilize the geometric phase method [96, 97] to guide the selection of a time-dependent driving field for the target atom. This approach enables a flexible choice of paths in the parameter space, allowing for efficient implementation of the desired quantum gate and offering greater versatility in system design and control optimization [98–100].

The remainder of this paper is structured as follows. In Sec. II, we introduce a parity-controlled gate that incorporates a geometric phase, achieved through the interaction of two control atoms and one target atom. We establish the relationships among detuning, dipole-dipole interactions, and Rabi frequencies, providing a clear representation of the effective model. In Sec. III, we conduct a comprehensive error analysis, exploring how parity-controlled gates are affected by vdW interactions between Rydberg states, atomic position fluctuations, laser phase effects, and Rabi amplitude noise. In Sec. IV, we discuss several applications of parity-controlled gates, including a one-step Rydberg parity meter compared to previous implementations, as well as the integration of repetition and surface codes, leveraging the advantages of single-shot measurements. Finally, in Sec. V, we summarize our findings and offer concluding remarks.

II. PARITY-CONTROLLED ARBITRARY GATES

A. Rydberg excitation engineering

We consider a two-dimensional square array [34, 79–81] composed of control atoms **C** and target atoms **T**, perpendicular to the quantization axis z determined by a static magnetic field B_z , in which three embedded Rydberg atoms are arranged linearly. As shown in Fig. 1(a), the control atoms **C1** and **C2** with the target atom **T3** are irradiated by a group of classical fields as shown in Fig. 1(b). For the control atoms, the transitions $|0\rangle \leftrightarrow |D\rangle$ and $|1\rangle \leftrightarrow |P\rangle$ are driven by lasers with the same real Rabi frequency Ω_c but opposite detuning Δ , while for the target atom, the transitions $|0\rangle \leftrightarrow |D\rangle(|P\rangle)$ and $|1\rangle \leftrightarrow |D\rangle(|P\rangle)$ are resonantly driven by lasers with complex Rabi frequencies Ω_0 ($|\Omega_0|e^{i\varphi_0}$) and Ω_1 ($|\Omega_1|e^{i\varphi_1}$), respectively. In the interaction picture, the corresponding Hamiltonian reads ($\hbar = 1$)

$$H = \sum_{n=1}^3 H_n + H_{\text{dd}}, \quad (1)$$

where

$$\begin{aligned} H_1 &= \Omega_c |D_1\rangle \langle 0_1| e^{-i\Delta t} + \Omega_c |P_1\rangle \langle 1_1| e^{i\Delta t} + \text{H.c.}, \\ H_2 &= \Omega_c |D_2\rangle \langle 0_2| e^{-i\Delta t} + \Omega_c |P_2\rangle \langle 1_2| e^{i\Delta t} + \text{H.c.}, \\ H_3 &= \Omega_0 (|D_3\rangle + |P_3\rangle) \langle 0_3| + \Omega_1 (|D_3\rangle + |P_3\rangle) \langle 1_3| + \text{H.c.}, \\ H_{\text{dd}} &= \sum_{i \neq j} J_{ij} |D_i\rangle \langle P_i| \otimes |P_j\rangle \langle D_j|, \end{aligned}$$

and $J_{ij} = C_3(1 - 3\cos^2\Theta)/d_{ij}^3$ is the dipole-dipole interaction strength between atoms i and j [101, 102], with Θ the polar angle concerning the quantization axis defined by the magnetic field. In the following, we assume the atomic spacing $d_{13} = d_{23} \equiv d$, corresponding to the dipole-dipole interaction strength $J_{13} = J_{23} = J$.

Under the condition $J = \Delta \gg \Omega_c \gg \{|\Omega_0|, |\Omega_1|\}$, we can obtain the effective form of Eq. (1) as

$$\begin{aligned} \mathcal{H} &= |0_1 0_2\rangle \langle 0_1 0_2| \otimes |D_3\rangle (\Omega_0 \langle 0_3| + \Omega_1 \langle 1_3|) \\ &\quad + |1_1 1_2\rangle \langle 1_1 1_2| \otimes |P_3\rangle (\Omega_0 \langle 0_3| + \Omega_1 \langle 1_3|) + \text{H.c.} \quad (2) \end{aligned}$$

The detailed derivation of Eq. (2) can be found in Appendix A. With this Hamiltonian, it is possible to derive a three-qubit parity-controlled gate through the integration of the dressed-state process [96, 97] that uses the nonadiabatic geometric way [103, 104] to engineer the dynamical evolution. If the conditions $\Omega = \sqrt{|\Omega_0|^2 + |\Omega_1|^2}$, $|\Omega_0|/|\Omega_1| = \tan\theta/2$, and $\varphi = \varphi_1 - \varphi_0$ are met, Eq. (2) could be rewritten as

$$\mathcal{H} = \Omega e^{i\varphi_1} |00D\rangle \langle 00b| + \Omega e^{i\varphi_1} |11P\rangle \langle 11b| + \text{H.c.}, \quad (3)$$

where we have used the notation $|ijk\rangle \langle ijk| = |i_1\rangle \langle i_1| \otimes |j_2\rangle \langle j_2| \otimes |k_3\rangle \langle k_3|$ for simplicity, and the ground state basis $|b\rangle = \sin\theta/2 e^{i\varphi} |0\rangle + \cos\theta/2 |1\rangle$ for atom **T3** and

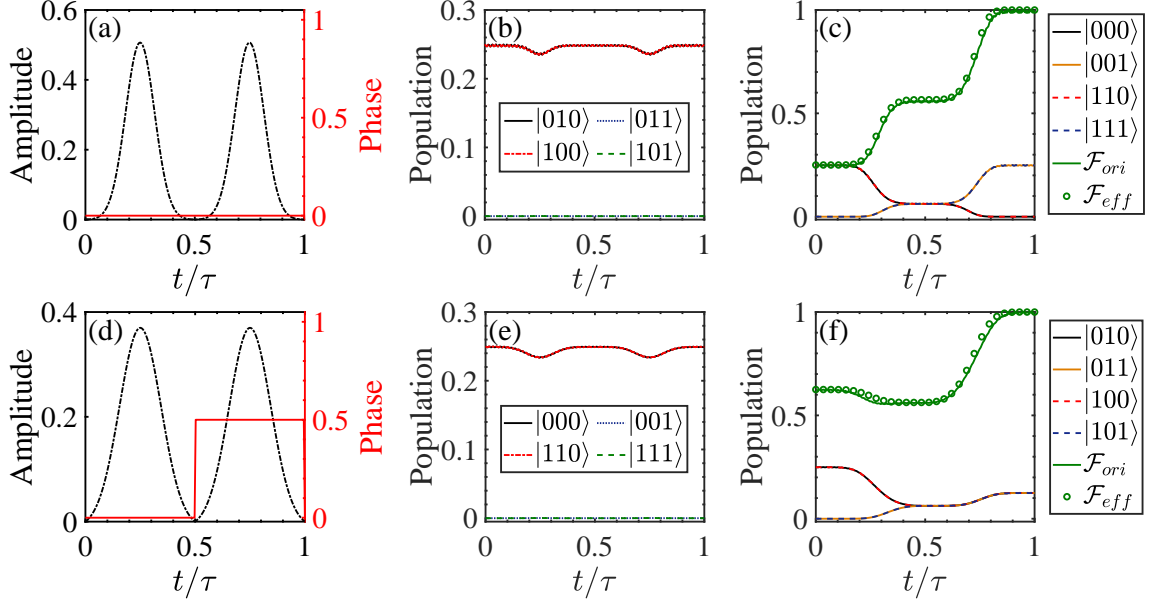


FIG. 2. The upper panel and the lower panel display, separately, evolution details of gates $PE-X$ and $PO-\sqrt{X}$. (a) and (d) are pulse envelopes with unit 2π MHz and phases with unit π , where the pulses are chosen to begin and end at zero to minimize errors as much as possible. (b) and (e) show the populations of virtually excited ground states. (c) and (f) show the populations of other ground states and fidelity comparison between the original and effective Hamiltonians, where \mathcal{F}_{ori} denotes the fidelity obtained from the original Hamiltonian and \mathcal{F}_{eff} denotes the fidelity obtained from the effective Hamiltonian.

the corresponding orthogonal dark one $|d\rangle = \cos\theta/2|0\rangle - \sin\theta/2e^{-i\varphi}|1\rangle$. To build a single-loop quantum gate, we divide the evolution time τ into two halves and choose $\varphi_1 = 0$ for $t \in [0, \tau/2)$ and $\varphi_1 = \pi - \gamma$ for $t \in [\tau/2, \tau]$, respectively. Thus, the Hamiltonians of Eq. (3) can be divided into $\mathcal{H}_A = \Omega(|00D\rangle\langle 00b| + |11P\rangle\langle 11b| + \text{H.c.})$ and $\mathcal{H}_B = -\Omega(e^{-i\gamma}|00D\rangle\langle 00b| + e^{-i\gamma}|11P\rangle\langle 11b| + \text{H.c.})$, leading to the effective geometric evolution operation $\mathcal{U}_E(\gamma, \theta, \varphi) = \exp(-i \int_0^\tau \mathcal{H} dt) = (|00\rangle\langle 00| + |11\rangle\langle 11|) \otimes U + (|01\rangle\langle 01| + |10\rangle\langle 10|) \otimes I$ with I being the identity operator. The overall evolution time τ is derived from the condition $\int_0^\tau \Omega dt = \pi$ and the single-qubit evolution operation is written as $U(\gamma, \theta, \varphi) = |d\rangle\langle d| + e^{i\gamma}|b\rangle\langle b| = \exp(i\gamma/2) \exp(-i\gamma/2 \mathbf{n} \cdot \boldsymbol{\sigma})$ in atom 3, with $\mathbf{n} = (-\sin\theta \cos\varphi, \sin\theta \sin\varphi, \cos\theta)$ and the Pauli operator $\boldsymbol{\sigma} = (X, Y, Z)$. In addition, if we change the laser driving to $|0_2\rangle \xleftrightarrow{\Omega_c} |P_2\rangle$ with red detuning Δ and $|1_2\rangle \xleftrightarrow{\Omega_c} |D_2\rangle$ with blue detuning Δ on the atom **C2** while doing nothing on the atoms **C1** and **T3**, we are able to get an odd parity-controlled gate $\mathcal{U}_O(\gamma, \theta, \varphi) = (|00\rangle\langle 00| + |11\rangle\langle 11|) \otimes I + (|01\rangle\langle 01| + |10\rangle\langle 10|) \otimes U$.

B. Effectiveness verification

We choose ground states $|0\rangle \equiv |5S_{1/2}, F=2, m_F=0\rangle$ and $|1\rangle \equiv |5S_{1/2}, F=2, m_F=2\rangle$, both of which can be coupled to the Rydberg state $|D\rangle \equiv |nD_{5/2}, m_j=5/2\rangle$ with two-photon excitation [46, 105], and coupled to $|P\rangle \equiv |n'P_{3/2}, m_j=3/2\rangle$ with single-photon excitation [106–111]

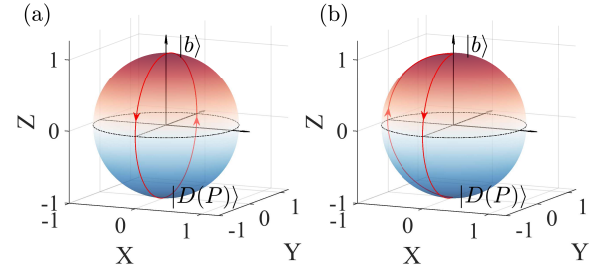


FIG. 3. Diagrams showing the rotation on atom **T3** for Pauli X (a) supplied by $U(\pi, \pi/2, \pi)$, and \sqrt{X} (b) given by $U(\pi/2, \pi/2, \pi)$. The two rotation operations always begin and end at the $|b\rangle$ (north pole), passing through the $|D(P)\rangle$ (south pole) in the process. The evolution trajectories on the Bloch sphere are enclosed in a circle (orange-slice-shaped path), with the open angle controlled by the geometric phase.

or three-photon excitation [112–116]. Similarly, excitation $|0\rangle \leftrightarrow |D\rangle$ (and $|1\rangle \leftrightarrow |P\rangle$) with blue (or red) detuning Δ for the control atoms can be executed.

The Rabi frequency Ω_c is set to be time-independent, while Ω_0 and Ω_1 are time-dependent, such that each segment of $\Omega(t)$ follows a Gaussian pulse

$$\Omega(t) = \begin{cases} \Omega_f [e^{-\frac{(t-2T)^2}{2(\alpha T)^2}} - a]/(1-a), & 0 < t \leq 4T \\ \Omega_f [e^{-\frac{(t-6T)^2}{2(\alpha T)^2}} - b]/(1-b), & 4T < t \leq \tau \end{cases} \quad (4)$$

with the maximum value Ω_f being independent of time, $T = \tau/8$, $a = \exp\{-2(T)^2/[2(\alpha T)^2]\}$, and $b = \exp\{-(\tau/2 - 6T)^2/[2(\alpha T)^2]\}$ ensuring the amplitude is zero at the start and end [117]. This Gaussian time-dependent soft control can effectively mitigate the impact of off-resonant terms, even at higher driving intensities, compared to time-independent driving [118]. For the numerical simulation evaluated by Schrödinger equation of Eq. (1), we initialize the system with the state $|\psi_0\rangle = 1/2(|0_1\rangle + |1_1\rangle) \otimes (|0_2\rangle + |1_2\rangle) \otimes |0_3\rangle$, and the temporal evolution of fidelity, denoted as $\mathcal{F} = |\langle\psi_0|\mathcal{U}_{\mathcal{E}(\mathcal{O})}^\dagger|\psi(t)\rangle|^2$, is measured by the population dynamics of the target state. To determine the optimal parameters Ω_c , Ω_f , and α without accounting for noise, we begin by presetting $\Omega_c = 2\pi \times 4.3$ MHz, $J = \Delta = 20\Omega_c$, the evolution duration $\tau = 3$ μ s, $\Omega_f = 2\pi \times 0.4$ MHz, and $\alpha = 0.3$. With fixed J , Δ , and τ , we then search for the optimal values of Ω_c , Ω_f , and α , by minimizing the cost function $1 - \mathcal{F}$. This optimization is performed using the minimize function in Python or `fmincon` in MATLAB. As a result, the optimized parameters are found to be $\Omega_c = 2\pi \times 3.533$ MHz, $\Omega_f = 2\pi \times 0.5069$ MHz, and $\alpha = 0.529$ for the even parity-controlled rotation $PE-X$ [$\equiv \mathcal{U}_{\mathcal{E}}(\pi, \pi/2, \pi)$], and $\Omega_c = 2\pi \times 2.3455$ MHz, $\Omega_f = 2\pi \times 0.3699$ MHz, and $\alpha = 0.7584$ for the odd parity-controlled rotation $PO-\sqrt{X}$ [$\equiv \mathcal{U}_{\mathcal{O}}(\pi/2, \pi/2, \pi)$]. In the following section, these parameters will be re-optimized to account for realistic experimental conditions. Figure 2 presents both pulses and populations versus time. Specifically, Figs. 2(a) and 2(d) depict the pulse amplitudes $\Omega(t)$ and phases $\varphi_1(t)$, respectively. These results correspond to $PE-X$ on atom **T3** with the evolution operation $U(\pi, \pi/2, \pi)$ and $PO-\sqrt{X}$ on the same atom with $U(\pi/2, \pi/2, \pi)$. For clarity, the rotation operations applied to the atom **T3** are illustrated in Fig. 3. Figures 2(b)-2(c) and 2(e)-2(f) display the population evolution for each computational basis, while the corresponding fidelities for the original and effective systems are presented in Figs. 2(c) and 2(f). The observed changes in the consistency of the fidelity curves highlight the effectiveness of the proposed scheme. Furthermore, we find that the atoms **C1**, **C2** always stay in the ground states, for example, in the case of $PE-X$, the ground states $\{|010\rangle, |011\rangle, |100\rangle, |101\rangle\}$ are almost unchanged except for slight oscillations while the ground states $\{|000\rangle, |001\rangle, |110\rangle, |111\rangle\}$ only have mutual exchange, which corresponds to the effective Hamiltonian in Eq. (2).

III. DISCUSSION OF THE EXPERIMENTAL FEASIBILITY

To facilitate the experimental implementation of our scheme, we can employ $|D\rangle = |79D_{5/2}, j = 5/2, m_j = 5/2\rangle$ and $|P\rangle = |80P_{3/2}, j = 3/2, m_j = 3/2\rangle$ [46, 105, 120], thus the corresponding $C_3 = 2\pi \times 13.0525$ GHz μm^3 [121] and atomic distance $d = 5.334$ μm under the circumstance $\Theta = \pi/2$. This determines the type and magnitude of general errors. Next, we attempt to propose experimentally feasible parameters to ensure that the parity-controlled gate is carried

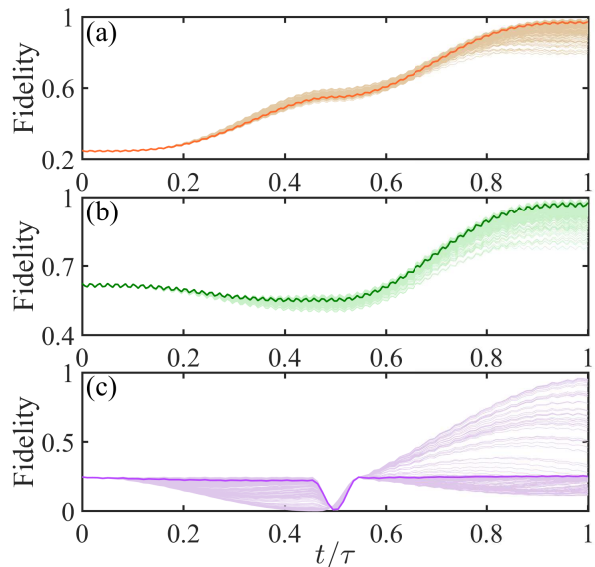


FIG. 4. Fidelities against position fluctuations for gates $PE-X$ (a) and $PO-\sqrt{X}$ (b) simulated by Monte Carlo integration [119], where each light-colored line denotes fidelity \mathcal{F} subjected to different position fluctuations and a bright-colored line denotes average fidelity $\bar{\mathcal{F}}$ with the initial state $|\psi(0)\rangle = 1/2(|00\rangle + |01\rangle + |10\rangle + |11\rangle) \otimes |0\rangle$. (c) is the fidelity in Ref. [18] against position fluctuations. Here we set $\mathcal{F} = |\langle\psi(\tau)|\psi(t)\rangle|^2$ and initial state $|\psi(0)\rangle = 1/(2\sqrt{2})(|00\rangle + |01\rangle + |10\rangle + |11\rangle) \otimes (|0\rangle + |1\rangle)$.

out without being significantly affected by random or specific errors in a realistic experimental setup. Here, we mainly discuss four kinds of noise, including atomic position fluctuations, laser phase noise, Rabi amplitude noise, and spontaneous emission from Rydberg states. Additionally, we must account for vdW interactions, which naturally exist in real systems. Fortunately, they only affect the modification of the Stark shifts of atoms **T3** with $\Omega_c^2/(\Delta - V_{13}^D) + \Omega_c^2/(\Delta - V_{23}^D) - 2\Omega_c^2/\Delta$ on $|D\rangle$ and $\Omega_c^2/(\Delta + V_{13}^P) + \Omega_c^2/(\Delta + V_{23}^P) - 2\Omega_c^2/\Delta$ on $|P\rangle$, with $V_{ij}^{D(P)}$ being the vdW interaction strength between Rydberg atoms i and j (see Appendix B). It should be noted that, in our scheme, the condition $J = \Delta$ is reminiscent of the Rydberg antiblockade mechanism. However, since the Rydberg double-excitation states are virtually excited, the scheme offers some robustness against fluctuations in atomic spacing. Despite this, position fluctuation errors remain the primary factor influencing the performance of this scheme, especially compared to the Rydberg blockade. To address this, we will perform a new numerical optimization based on the specific experimental parameters of the optical traps. The resulting optimized parameter set will also be used to evaluate other experimental errors.

Atomic position fluctuations. Atomic position fluctuations, which come from factors such as optical trap and atomic temperature, present a challenge during pulse sequences when the traps are turned off [122]. To model the effects of these fluctuations, we first assume three optical traps that confine atoms **C1**, **C2**, and **T3**, with the trap centers located at $(-d, 0, 0)$, $(d, 0, 0)$, and $(0, 0, 0)$, respectively. Due to the finite trap

depths, the atomic positions exhibit fluctuations. We denote the perturbed positions of the atoms by $(-d + \sigma_{x1}, \sigma_{y1}, \sigma_{z1})$ for **C1**, $(d + \sigma_{x2}, \sigma_{y2}, \sigma_{z2})$ for **C2**, and $(\sigma_{x3}, \sigma_{y3}, \sigma_{z3})$ for **T3**, where $\sigma_{xi}, \sigma_{yi}, \sigma_{zi}$ represent the deviations in positions along each axis for atom i . The actual dipole-dipole interaction can be calculated by interatomic distances

$$d_{13} = \{[\sigma_{x3} - (\sigma_{x1} - d)]^2 + (\sigma_{y3} - \sigma_{y1})^2 + (\sigma_{z3} - \sigma_{z1})^2\}^{1/2},$$

$$d_{12} = \{[(\sigma_{x2} + d) - (\sigma_{x1} - d)]^2 + (\sigma_{y2} - \sigma_{y1})^2 + (\sigma_{z2} - \sigma_{z1})^2\}^{1/2},$$

$$d_{23} = \{[(\sigma_{x2} + d) - \sigma_{x3}]^2 + (\sigma_{y2} - \sigma_{y3})^2 + (\sigma_{z2} - \sigma_{z3})^2\}^{1/2}.$$

In Ref. [123], researchers demonstrated ultrafast energy exchange between two single Rydberg atoms using an optical trap with a depth of $|\text{U}_m| = 0.62$ mK. The corresponding trap frequencies are $(\omega_x, \omega_y, \omega_z) = 2\pi \times (147, 117, 35)$ kHz, with mean motional quanta $\bar{n}_{x,y,z} = (0.11, 0.11, 0.56)$, and the position fluctuation $\sigma_{x,y,z} = (22, 25, 60)$ nm. To simulate the effects of these fluctuations, we use Monte Carlo integration [119] for numerical simulation. The random number of each atom subject to the Gaussian distribution can be generated with two uniformly distributed random numbers ζ_1 and ζ_2 in the interval $[0, 1]$, denoted as $\sigma_{x(y,z)}\sqrt{-2\ln\zeta_1}\cos 2\pi\zeta_2$ [47]. We define the average fidelity as $\bar{\mathcal{F}} = 1/\mathcal{N}\sum_{n=1}^{\mathcal{N}}\mathcal{F}_n$, where the initial state is set as $|\psi(0)\rangle = 1/2(|00\rangle + |01\rangle + |10\rangle + |11\rangle) \otimes |0\rangle$. The state $|\psi(t)\rangle$ is derived from the Schrödinger equation $i\frac{\partial}{\partial t}|\psi(t)\rangle = H(\boldsymbol{\sigma}^1, \boldsymbol{\sigma}^2, \boldsymbol{\sigma}^3, t)|\psi(t)\rangle$, where the superscripts 1, 2, and 3 denote the atoms **C1**, **C2**, **T3**, and $\boldsymbol{\sigma} \equiv (\sigma_x, \sigma_y, \sigma_z)$. Combining the dipole-dipole interaction and the vdW interaction influenced by position fluctuation and the preset parameters in Sec. II B, by minimizing the cost function $1 - \bar{\mathcal{F}}$, we obtain the optimal parameters $\Omega_c = 2\pi \times 5$ MHz, $\Omega_f = 2\pi \times 0.248$ MHz, and $\alpha = 42.76$ for gate *PE-X* as well as $\Omega_c = 2\pi \times 5$ MHz, $\Omega_f = 2\pi \times 0.2459$ MHz, and $\alpha = 42.7456$ for gate *PO-√X*. We find the average fidelity $\bar{\mathcal{F}} = 0.9731$ for operations *PE-X* and $\bar{\mathcal{F}} = 0.9773$ for *PO-√X*, as illustrated in Figs. 4(a) and 4(b). Using identical trap parameters, we compare the results with those of Ref. [18] under similar position fluctuations for the initial state $|\psi(0)\rangle = 1/(2\sqrt{2})(|00\rangle + |01\rangle + |10\rangle + |11\rangle) \otimes (|0\rangle + |1\rangle)$. It can be observed that the fidelity depicted in Fig. 4(c) decreased significantly, primarily due to disruption of the Rydberg antiblockade and phase confusion caused by the vdW interaction in the target state.

Two additional factors should be highlighted: First, the anisotropy of Rydberg interactions, including dipole-dipole and vdW interactions between states $|D\rangle$ and $|P\rangle$, is neglected due to the minimal variations in angle Θ resulting from atomic position fluctuations. Second, reducing the atomic temperature decreases position uncertainty, thus enhancing the fidelity. In particular, recent studies have shown that Rydberg atoms can be cooled to temperatures below $5 \mu\text{K}$ [124–126].

Laser phase error. Another important effect that contributes to the damping of oscillations is the finite-phase noise present

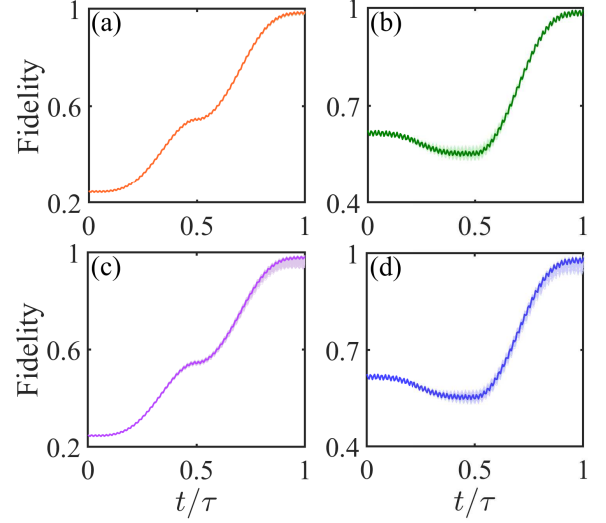


FIG. 5. Fidelities against laser phase noise for gates *PE-X* (a) and *PO-√X* (b), and against Rabi amplitude noise for gates *PE-X* (c) and *PO-√X* (d) simulated by Monte Carlo integration [119], where each light-colored line denotes fidelity \mathcal{F} subjected to different noises and a bright-colored line denotes average fidelity $\bar{\mathcal{F}}$ with the initial state $|\psi(0)\rangle = 1/2(|00\rangle + |01\rangle + |10\rangle + |11\rangle) \otimes |0\rangle$.

in the excitation lasers [55, 127, 128]. Here we draw on the discussion in Ref. [55] and use Monte Carlo to simulate the impact of phase noise [128]. Each beam is power stabilized $< 1\%$ by an acousto-optic modulator in Ref. [55]; thus, we assume the laser phase noise of $\Delta\phi_c = \Delta\phi = 0.01\pi$ (standard deviation). All beams consider different random sampling results, while two control atoms use the same random sampling results in the case *PE-X*. The numerical result is shown in Figs. 5(a) and 5(b) with fidelities of 0.9891 for gate *PE-X* and 0.9934 for *PO-√X*; we find that fidelity is only slightly affected within such a fluctuation due to the precise control of laser phase.

Rabi amplitude noise. The deviation of atoms from the center of the laser due to slight position shifts caused by the finite beam waist, or power drifts of the laser field, raises concerns regarding Rabi amplitude noise [47, 48, 129–131]. For the sake of discussion, we assume that these inhomogeneities can be represented as $(1 + \epsilon_i)\Omega_i$ [48], where the standard deviation ϵ_i signifies the error rate associated with Ω_i . Specifically, we delineate the situation into two categories: $(1 + \epsilon_c)\Omega_c$ and $(1 + \epsilon)\Omega$, and we set $\epsilon_c = \epsilon = 0.008$ [131]. Similarly, all beams still consider different random sampling results, while two control atoms use the same random sampling results in the case *PE-X*. The numerical results are presented in Figs. 5(c) and 5(d) with fidelities of 0.9837 for gate *PE-X* and 0.9868 for gate *PE-√X*. It can be observed that this error has a certain influence on the parity-controlled gates. However, its relatively minor impact can be attributed to advances in current experimental technology.

In addition, we also point out that the numerical results are largely unaffected by errors originating from the Rabi frequency Ω_c and phase ϕ_c for gates *PE-X* and *PO-√X*.

This robustness arises from the reliance of the scheme on the condition $\Delta \gg \Omega_c \gg \{|\Omega_0|, |\Omega_1|\}$, which does not impose strict numerical constraints on Ω_c and ϕ_c . Upon applying the rotation framework U_{rc} as described in Appendix A, we observe that the coupling terms between ground and excited states, associated with $\Omega_c \exp(i\phi_c)$, are discarded due to high-frequency oscillations. Consequently, the couplings driven by Ω_c and ϕ_c do not dominate the effective evolution of the system, making it highly resistant to errors. In contrast, errors associated with $\Omega(t)$ and ϕ significantly impact the fidelity of $PE-X$ or $PO-\sqrt{X}$. This is mainly because the effective Hamiltonian of Eq. (2) is closely related to the parameter $\Omega(t)$, which directly affects the performance of the gates.

Spontaneous emission. At the beginning, for the sake of clarity in our discussion, we introduce an uncoupled state $|m\rangle$ to encompass all ground states apart from the computational basis states. According to the Alkali-Rydberg-Calculator toolbox [121], the lifetimes (in temperature $5 \mu\text{K}$) are $\tau_S = 1/\gamma_D = 508 \mu\text{s}$ for the Rydberg state $|D\rangle$ and $\tau_P = 1/\gamma_P = 1140 \mu\text{s}$ for state $|P\rangle$, and the branching ratios to dissipate the ground state manifolds are $b_{0(1)D} = b_{0(1)P} = 1/8$ and $b_{mD} = b_{mP} = 3/4$. The temporal evolution of the system considering atomic decay is governed by the Lindblad master equation,

$$\frac{d\rho}{dt} = i[\rho(t), H(t)] + \sum_{k=D,P} \mathcal{L}_k[\rho], \quad (5)$$

where

$$\mathcal{L}_k[\rho] = \sum_{n=1,2,3} \sum_{i=m,0,1} L_{ik}^{(n)} \rho L_{ik}^{(n)\dagger} - \frac{1}{2} \{L_{ik}^{(n)\dagger} L_{ik}^{(n)}, \rho\}$$

is the Lindblad operator describing spontaneous emission of Rydberg states $|D_n\rangle$ and $|P_n\rangle$, with $L_{ik}^{(n)} = \sqrt{b_{ik}\gamma_k} |i_n\rangle \langle k_n|$. The temporal evolution of fidelity \mathcal{F} with Eq. (5) is changed to $\mathcal{F} = \langle \psi(\tau) | \rho(t) | \psi(\tau) \rangle$. The numerical simulation is displayed in Figs. 6(a) and 6(b) with fidelities of 0.9921 (decay) and 0.9927 (no error) for gate $PE-X$, 0.9933 (decay) and 0.9941 (no error) for gate $PO-\sqrt{X}$. We find that the error caused by spontaneous emission is hardly affected regardless of whether the gate is $PE-X$ or $PO-\sqrt{X}$.

On balance, we also consider the influence of all errors including the vdW interactions, atomic position fluctuations, laser phase error, Rabi amplitude noise, and spontaneous emission for gates $PE-X$ or $PO-\sqrt{X}$ as shown in Fig. 7. The fidelity is about 96.61% for gates $PE-X$ and 96.97% for gates $PO-\sqrt{X}$.

IV. APPLICATIONS OF PARITY-CONTROLLED GATE

Parity meter. The effective evolution operation $U_{\mathcal{E}} = (|00\rangle\langle 00| + |11\rangle\langle 11|) \otimes U + (|01\rangle\langle 01| + |10\rangle\langle 10|) \otimes I$ is a geometric gate controlled by parity, which performs the operation U on an atom $\mathbf{T3}$ when the parity of the control atoms is even, while it does nothing for an atom $\mathbf{T3}$ when odd parity. One of

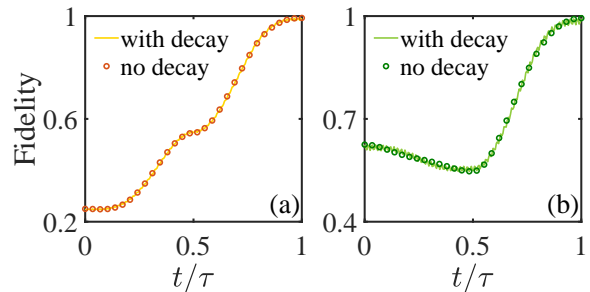


FIG. 6. Fidelities against spontaneous emission for gates $PE-X$ (a) and $PO-\sqrt{X}$ (b). A solid line represents fidelity in the presence of decay, while a hollow circle represents fidelity without decay. There is no obvious difference between them.

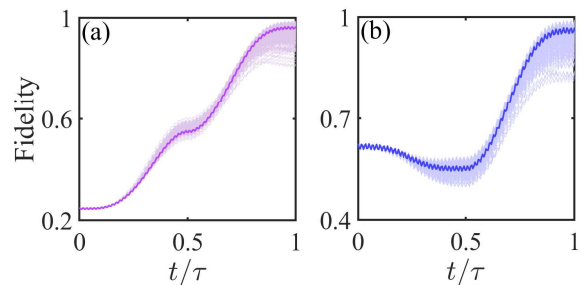


FIG. 7. Fidelities after considering the vdW interactions, atomic position fluctuations, laser phase error, Rabi amplitude noise, and spontaneous emission for gates $PE-X$ (a) and $PO-\sqrt{X}$ (b). The parameters can be found in Sec. III.

the most basic applications of the model is the Rydberg parity meter. Now we regard the atom $\mathbf{T3}$ as an auxiliary qubit and check the parity of the atoms $\mathbf{C1}$ and $\mathbf{C2}$. We can easily determine even or odd parity by the dynamical evolution of the auxiliary atom $\mathbf{T3}$, as mentioned above. The processing time of $3 \mu\text{s}$ provided by our measurement is much less than $19.11 \mu\text{s}$ in [19] with comparable maximum Rabi frequencies. Additionally, a comparison of our suggested method's robustness against position fluctuations in Fig. 4 and the parity meters covered in Ref. [18] shows a significant improvement.

Three-qubit repetition code. The logical state of this three-qubit repetition code is

$$|\psi\rangle_L = \mathcal{A}|000\rangle + \mathcal{B}|111\rangle \equiv \mathcal{A}|0\rangle_L + \mathcal{B}|1\rangle_L, \quad (6)$$

where the logical codewords $|0\rangle_L = |000\rangle$ and $|1\rangle_L = |111\rangle$, which can be used to correct the single-qubit flip error under such a set of basis vectors. A bit-flip error X_2 affecting only the second qubit results in

$$X_2|\psi\rangle_L = \mathcal{A}|010\rangle + \mathcal{B}|101\rangle. \quad (7)$$

Equation (7) corresponds to the error subspace $\mathcal{Q} = \text{span}\{|100\rangle, |011\rangle, |010\rangle, |101\rangle, |001\rangle, |110\rangle\}$ transformed from the codespace $\mathcal{C} = \text{span}\{|000\rangle, |111\rangle\}$, with \mathcal{C} and \mathcal{Q} being orthogonal. Therefore, the syndrome extraction can be performed using the orthogonality of two subspaces.

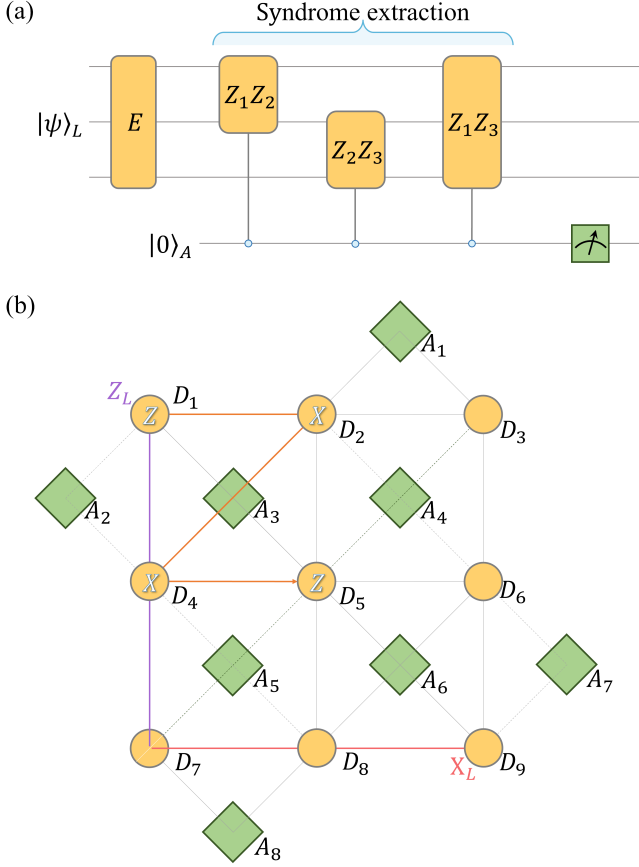


FIG. 8. (a) Syndrome check of three-qubit repetition code. E denotes an error that occurs in the quantum circuit. Subsequently, the three stabilizers, Z_1Z_2 , Z_2Z_3 , and Z_1Z_3 implemented by $PO-\sqrt{X}$ gate are applied to perform syndrome extraction. The error result is determined by the result of the single-shot measurement of the ancilla. (b) Syndrome check of $[[9, 1, 3]]$ rotated surface code. The yellow circle denotes a data qubit D_i and the red square denotes an ancillary qubit A_i , which are described by the control atoms \mathbf{C} and target atoms \mathbf{T} , respectively. The four-qubit stabilizer $XZZX$ can be realized in twice parity-controlled gate operations without replacement of auxiliary atoms.

As shown in Fig. 8(a), we use the stabilizer operator Z_iZ_j to check the parity between the data qubits i and j [82]. After an error stage represented by the circuit element $E \in \{I, X_1, X_2, X_3\}$, we consistently observe that two stabilizer prompts exhibit errors, while one stabilizer prompt remains error-free. This strategy has been used in combination with 2-designs to improve the fault tolerance of error correction circuits [132]. In addition, its combination with our odd parity-controlled gate $PO-\sqrt{X}$ will yield even more unexpected results. When an error occurs as in Eq. (7), two stabilizers will consistently show odd-parity behavior, while the remaining stabilizer will exhibit even-parity behavior. The obvious advantage of employing the $PO-\sqrt{X}$ scheme is that we only need one ancillary qubit and measure the ancillary qubit once throughout the process [25]. After threading three stabilizers Z_iZ_j , there are consistently two

\sqrt{X} operations, resulting in $\sqrt{X} \cdot \sqrt{X} = X$, so that the syndrome extraction $+1$ corresponds to the encoding space, while -1 corresponds to the error space. The repetition code corrects not only X -type errors, but also Z -type errors. To enable this, the computational basis must be transformed from $\{|0\rangle, |1\rangle\}$ to $\{|+\rangle, |-\rangle\}$, where $|+\rangle = (|0\rangle + |1\rangle)/\sqrt{2}$ and $|-\rangle = (|0\rangle - |1\rangle)/\sqrt{2}$. This transformation involves modifying the model in Fig. 1(b) by introducing two additional transitions: $|S\rangle \leftrightarrow |1\rangle$ with Ω_c and $|P\rangle \leftrightarrow |0\rangle$ with $-\Omega_c$. Combining these transitions yields effective couplings $|S\rangle \leftrightarrow |+\rangle$ and $|P\rangle \leftrightarrow |-\rangle$, with a Rabi frequency of $\sqrt{2}\Omega_c$. As a result, the computational basis changes from $\{|0\rangle, |1\rangle\}$ to $\{|+\rangle, |-\rangle\}$.

Surface code. The surface code plays an important role in QEC [8, 16, 27–29, 133–136]. Unlike previous approaches that relied on CZ for stabilizer syndrome, we utilize alternative parity-controlled gates to achieve this task in Rydberg atoms. This, in turn, simplifies the number of gates and operational steps needed for the extraction of the stabilizer syndrome. As shown in Fig. 8(b), we give the rotated $XZZX$ surface code $[[9, 1, 3]]$ with 9 being the total number of bits per codeword, 1 being the number of encoded bits and 3 being the code distance, which is the smallest surface code capable of detecting and correcting errors and can be represented as a single logical qubit. The symbol D_i denotes the i th data qubit and A_i denotes the ancillary one. Consequently, we have the logical Z_L operation $Z_{D_1}Z_{D_4}Z_{D_7}$ and the logical X_L operation $X_{D_2}X_{D_5}X_{D_8}$. In this paper, our main focus lies on the error detection process. Specifically, we illustrate the application of our even parity-controlled gate $PE-X$ within the surface code using example stabilizers $Z_{D_1}X_{D_2}X_{D_4}Z_{D_5}$ with an auxiliary qubit A_3 . The parity-controlled gate can check the parity of two atoms, thus, we need two steps to finish the extraction of four stabilizer syndromes. We can measure $Z_{D_1}Z_{D_5}$ and then $X_{D_2}X_{D_4}$ (the computational basis once again needs to be transformed from $\{|0\rangle, |1\rangle\}$ to $\{|+\rangle, |-\rangle\}$). The parities of the dual measurements coincide with the outcome of the ultimate stabilizer measurement. Specifically, an odd count of occurrences with odd parity corresponds to -1 , while an even count with odd parity corresponds to $+1$. For example, considering the four-atom state $|\psi\rangle_{\text{four}} = (|0+ -0\rangle_{1245} + |1- +1\rangle_{1245})/\sqrt{2}$, we obtain the stabilizer $Z_1X_2X_4Z_5$ result as -1 . Among them, we notice that the stabilizer check process is similar to the repetition code one, which does not require the re-initialization of ancillary atoms during the two parity-controlled gates.

V. SUMMARY

The proposed approach presents a method for implementing a parity-controlled gate using spin-exchange dipole-dipole interactions between Rydberg atoms. This quantum gate demonstrates a degree of error resilience by effectively utilizing virtual excitations into Rydberg states of control atoms and leveraging the robustness offered by geometric phases. The efficiency of our parity meter is evident in its simplified procedure and enhanced processing speed, outperform-

ing previous Rydberg-based parity methods. It is applied to three-qubit repetition codes and rotated surface codes in the $XZZX$ architecture, demonstrating its versatility. By strategically manipulating additional atoms during parity measurements, we can obtain immediate readings of stabilizers in these codes. Furthermore, our analytical implementation of the parity-controlled gate provides deeper insights into the physical problem, offering a clearer understanding of how atom-light interactions influence the outcome. It can also be generalized to other quantum tasks, such as one-step multipartite controlled-NOT gates and the purification of multipartite entangled states, thus expanding the toolkit for quantum information processing with Rydberg atoms. These applications will be explored further in our future research, and we look forward to the experimental realization of our approach.

VI. ACKNOWLEDGMENT

The authors gratefully acknowledge the anonymous reviewers for their careful review and valuable suggestions, which have significantly improved the clarity and readability of the manuscript. This work was supported by the National Natural Science Foundation (Grant Nos. 12174048 and 12274376), a major science and technology project of Henan Province under Grant No. 221100210400, and the National Science Foundation of Henan Province under Grant No. 212300410085. W.L. acknowledges support from the EPSRC through Grant No. EP/W015641/1 and the Going Global Partnerships Programme of the British Council (Contract No. IND/CONT/G/22-23/26)

VII. AUTHOR CONTRIBUTIONS

X.Q.S. conceptualized the study. F.Q.G. drafted the manuscript and conducted data analysis under the guidance of S.L.S., W.B.L., and X.Q.S. All authors contributed to the review and editing of the manuscript.

Appendix A: Derivation of effective Hamiltonian

By extending the dipole-dipole interaction into three-atom direct product states, we have

$$H_{\text{dd}} = H_{\text{dd}}^1 + H_{\text{dd}}^2, \quad (\text{A1})$$

where

$$\begin{aligned} H_{\text{dd}}^1 = & J(|DDP\rangle\langle PDD| + |DPP\rangle\langle PPD| + |DDP\rangle\langle DPD| \\ & + |PDP\rangle\langle PPD|) + J_{12}(|DPD\rangle\langle PDD| \\ & + |DPP\rangle\langle PDP|) + \text{H.c.}, \end{aligned}$$

$$H_{\text{dd}}^2 = \sum_{\Lambda=0,1} J(|D\Lambda P\rangle\langle P\Lambda D| + |\Lambda DP\rangle\langle \Lambda PD|)$$

$$+ J_{12}|DPA\rangle\langle PDA| + \text{H.c.} \quad (\text{A2})$$

Indeed, there exists a splitting for Rydberg energy levels due to strong dipole-dipole interaction between two Rydberg atoms. Thus, we can diagonalize H_{dd} according to the subsystem. First, $H_{\text{dd}}^1 = H_{\text{dd}}^{1A} + H_{\text{dd}}^{1B}$ includes two subspaces $\{|DPD\rangle, |PDD\rangle, |DDP\rangle\}$ and $\{|DPP\rangle, |PDP\rangle, |PPD\rangle\}$. For H_{dd}^{1A} , we have

$$\begin{aligned} H_{\text{dd}}^{1A} &= \mathcal{E}_1|\mathcal{E}_1\rangle\langle\mathcal{E}_1| + \mathcal{E}_2|\mathcal{E}_2\rangle\langle\mathcal{E}_2| + \mathcal{E}_3|\mathcal{E}_3\rangle\langle\mathcal{E}_3|, \\ |\mathcal{E}_1\rangle &= -\frac{1}{\sqrt{2}}|DPD\rangle + \frac{1}{\sqrt{2}}|PDD\rangle, \\ |\mathcal{E}_2\rangle &= \frac{\mathcal{E}_2}{\sqrt{2\mathcal{E}_2^2 + 4J^2}}|DPD\rangle + \frac{\mathcal{E}_2}{\sqrt{2\mathcal{E}_2^2 + 4J^2}}|PDD\rangle \\ &\quad + \frac{2J}{\sqrt{2\mathcal{E}_2^2 + 4J^2}}|DDP\rangle, \\ |\mathcal{E}_3\rangle &= \frac{\mathcal{E}_3}{\sqrt{2\mathcal{E}_3^2 + 4J^2}}|DPD\rangle + \frac{\mathcal{E}_3}{\sqrt{2\mathcal{E}_3^2 + 4J^2}}|PDD\rangle \\ &\quad + \frac{2J}{\sqrt{2\mathcal{E}_3^2 + 4J^2}}|DDP\rangle, \end{aligned}$$

with eigenvalues $\mathcal{E}_1 = -J_{12}$, $\mathcal{E}_2 = \frac{1}{2}(J_{12} - \sqrt{8J^2 + J_{12}^2})$, and $\mathcal{E}_3 = \frac{1}{2}(J_{12} + \sqrt{8J^2 + J_{12}^2})$. Similarly, for H_{dd}^{1B} we have the same eigenvalues and the same eigenstates form with different bases $\{|DPP\rangle, |PDP\rangle, |PPD\rangle\}$.

Second, $H_{\text{dd}}^2 = H_{\text{dd}}^{2A} + H_{\text{dd}}^{2B} + H_{\text{dd}}^{2C}$ includes three subspaces, $\{|D\Lambda P\rangle, |P\Lambda D\rangle\}$, $\{|\Lambda DP\rangle, |\Lambda PD\rangle\}$, and $\{|DPA\rangle, |PDA\rangle\}$. For H_{dd}^{2A} , we have

$$\begin{aligned} H_{\text{dd}}^{2A} &= \mathcal{G}_1|\mathcal{G}_1\rangle\langle\mathcal{G}_1| + \mathcal{G}_2|\mathcal{G}_2\rangle\langle\mathcal{G}_2|, \\ |\mathcal{G}_1\rangle &= -\frac{1}{\sqrt{2}}|D\Lambda P\rangle + \frac{1}{\sqrt{2}}|P\Lambda D\rangle, \\ |\mathcal{G}_2\rangle &= \frac{1}{\sqrt{2}}|D\Lambda P\rangle + \frac{1}{\sqrt{2}}|P\Lambda D\rangle, \end{aligned}$$

with eigenvalues $\mathcal{G}_1 = -J$, $\mathcal{G}_2 = J$. Similarly, for H_{dd}^{2B} we have the same eigenvalues and the same eigenstates form with different bases $\{|\Lambda DP\rangle, |\Lambda PD\rangle\}$. While for H_{dd}^{2C} we have

$$\begin{aligned} H_{\text{dd}}^{2C} &= \mathcal{O}_1|\mathcal{O}_1\rangle\langle\mathcal{O}_1| + \mathcal{O}_2|\mathcal{O}_2\rangle\langle\mathcal{O}_2|, \\ |\mathcal{O}_1\rangle &= -\frac{1}{\sqrt{2}}|DPA\rangle + \frac{1}{\sqrt{2}}|PDA\rangle, \\ |\mathcal{O}_2\rangle &= \frac{1}{\sqrt{2}}|DPA\rangle + \frac{1}{\sqrt{2}}|PDA\rangle, \end{aligned}$$

with eigenvalues $\mathcal{O}_1 = -J_{12}$, $\mathcal{O}_2 = J_{12}$.

For brevity, we use the notion E_ν^μ to denote the μ th basis of ν subspace, where $\mu \in \{1, 2, 3\}$ and $\nu \in \{DPD, DPP, D\Lambda P, \Lambda DP, DPA\}$. Assuming the condition $J = \Delta \gg \{|\Omega_0|, |\Omega_1|, \Omega_c\}$, then a rotation $U_{rd} = \exp(-iH_{\text{dd}}t)$ is performed. The total Hamiltonian H after eliminating the high-frequency oscillating terms can be written as

$$H = H_{00} + H_{01} + H_{10} + H_{11}, \quad (\text{A3})$$

where

$$\begin{aligned} H_{00} &= \Omega_0|00D\rangle\langle 000| + \Omega_1|00D\rangle\langle 001| + \Omega_0|00P\rangle\langle 000| \\ &+ \Omega_1|00P\rangle\langle 001| + \frac{\Omega_c}{\sqrt{2}}|E_{D0P}^2\rangle\langle 00P| \\ &+ \frac{\Omega_c}{\sqrt{2}}|E_{0DP}^2\rangle\langle 00P| + \text{H.c.}, \\ H_{01} &= \Omega_0|01D\rangle\langle 010| + \Omega_1|01D\rangle\langle 011| \\ &+ \frac{\Omega_c}{\sqrt{2}}|E_{0DP}^1\rangle\langle 01D| + \Omega_0|01P\rangle\langle 010| \\ &+ \Omega_1|01P\rangle\langle 011| + \frac{\Omega_c}{\sqrt{2}}|E_{D1P}^2\rangle\langle 01P| + \text{H.c.}, \\ H_{10} &= \Omega_0|10D\rangle\langle 100| + \Omega_1|10D\rangle\langle 101| \\ &+ \frac{\Omega_c}{\sqrt{2}}|E_{D0P}^1\rangle\langle 10D| + \Omega_0|10P\rangle\langle 100| \\ &+ \Omega_1|10P\rangle\langle 101| + \frac{\Omega_c}{\sqrt{2}}|E_{1DP}^2\rangle\langle 10P| + \text{H.c.}, \\ H_{11} &= \Omega_0|11D\rangle\langle 110| + \Omega_1|11D\rangle\langle 111| \\ &+ \frac{\Omega_c}{\sqrt{2}}|E_{D1P}^1\rangle\langle 11D| + \frac{\Omega_c}{\sqrt{2}}|E_{1DP}^1\rangle\langle 11D| \\ &+ \Omega_0|11P\rangle\langle 110| + \Omega_1|11P\rangle\langle 111| + \text{H.c.} \end{aligned} \quad (\text{A4})$$

The Hamiltonian can be further reduced by the condition $\Omega_c \gg \{|\Omega_0|, |\Omega_1|\}$. For example, the strong transition term $\Omega_c/\sqrt{2}|E_{D0P}^1\rangle\langle 00P| + \Omega_c/\sqrt{2}|E_{0DP}^1\rangle\langle 00P| + \text{H.c.}$ with Ω_c is further diagonalized as $\lambda_1|\lambda_1\rangle\langle \lambda_1| + \lambda_2|\lambda_2\rangle\langle \lambda_2|$ with the eigenstates $|\lambda_1\rangle = (|E_{D0P}^1\rangle - \sqrt{2}|00P\rangle + |E_{0DP}^1\rangle)/2$, $|\lambda_2\rangle = (|E_{D0P}^1\rangle + \sqrt{2}|00P\rangle + |E_{0DP}^1\rangle)/2$, $|\lambda_0\rangle = (-|E_{D0P}^1\rangle + |E_{0DP}^1\rangle)/\sqrt{2}$, and the corresponding eigenvalues $\lambda_1 = -\sqrt{2}\Omega_c$, $\lambda_2 = \sqrt{2}\Omega_c$, $\lambda_0 = 0$. Thus, the terms $\Omega_0|00P\rangle\langle 000| + \Omega_1|00P\rangle\langle 001| + \text{H.c.}$ are transformed into $[-1/\sqrt{2}\exp(-i\sqrt{2}\Omega_c t)|\lambda_1\rangle + 1/\sqrt{2}\exp(i\sqrt{2}\Omega_c t)|\lambda_2\rangle](\Omega_0|000\rangle + \Omega_1|001\rangle) + \text{H.c.}$ after using the rotation frame $U_{rc} = \exp[-i(\lambda_1|\lambda_1\rangle\langle \lambda_1| + \lambda_2|\lambda_2\rangle\langle \lambda_2| + \lambda_0|\lambda_0\rangle\langle \lambda_0|)t]$ and then discarded due to high-frequency oscillation. Similar processing occurs on H_{01} , H_{10} , and H_{11} . As a result, the final Hamiltonian is as follows:

$$\begin{aligned} H_{\text{eff}} &= |00\rangle\langle 00| \otimes (\Omega_0|D\rangle\langle 0| + \Omega_1|D\rangle\langle 1|) \\ &+ |11\rangle\langle 11| \otimes (\Omega_0|P\rangle\langle 0| + \Omega_1|P\rangle\langle 1|) + \text{H.c.} \end{aligned} \quad (\text{A5})$$

Several techniques can be used to mitigate Stark shifts, including phase adjustments [137, 138], the use of auxiliary detuned transitions [139, 140], and the optimal determination of detunings [141, 142]. In the present case, additional lasers have been utilized to counteract the Stark shifts Ω_c^2/Δ that affect the control atoms **C1** and **C2**.

Appendix B: Influence of vdW interaction

The premise of our approach is that it relies exclusively on dipole-dipole interactions, rendering the vdW interaction of the relevant Rydberg states at atomic distance d [46] undesirable. In principle, this type of interaction can be ignored by expanding the interatomic distance, as done in Refs. [101, 102], which employ the distance between two atoms over $20 \mu\text{m}$ such that the vdW interaction remains on the order of kilohertz. Although our scheme cannot eliminate the vdW interaction by similar means, fortunately, we observe that it primarily affects certain unnecessary detunings that can be regarded as high-frequency oscillating terms in Eq. (A3). For clarity, an analytical discussion is provided below.

Taking into account the potential Rydberg interactions, the Hamiltonian of the system reads

$$H = \sum_{n=1}^3 H_n + H_{\text{dd}} + H_{\text{vdw}}, \quad (\text{B1})$$

where $H_{\text{vdw}} = \sum_{i < j} V_{ij}^D |D_i D_j\rangle\langle D_i D_j| + V_{ij}^P |P_i P_j\rangle\langle P_i P_j|$. Here, $V_{ij}^{D,P} = -C_6^{D,P}(\Theta, \Phi)/d_{ij}^6$ denotes the vdW interaction strength with angle (Θ, Φ) on a spherical basis. Specifically, $C_6^D(\pi/2, 0) = 2\pi \times 1542.60 \text{ GHz } \mu\text{m}^6$ for the Rydberg state $|79D_{5/2}, j = 5/2, m_j = 5/2\rangle$ and $C_6^P(\pi/2, 0) = 2\pi \times 5486.82 \text{ GHz } \mu\text{m}^6$ for $|80P_{3/2}, j = 3/2, m_j = 3/2\rangle$, resulting in $V_{13}^D = V_{23}^D = -2\pi \times 66.978 \text{ MHz}$, $V_{12}^D = -2\pi \times 1.0465 \text{ MHz}$, $V_{13}^P = V_{23}^P = -2\pi \times 238.23 \text{ MHz}$ and $V_{12}^P = -2\pi \times 3.7223 \text{ MHz}$. It is important to note that when considering these unwanted interactions, a reexamination of the Stark shifts in states $|00D\rangle$ and $|11P\rangle$ is necessary. For Hamiltonian components H_{00} and H_{11} in Appendix A, these interactions alter the detunings of states $|00D\rangle$ and $|11P\rangle$, thereby impacting the previous scheme to eliminate Stark shifts on atoms **C1** and **C2**. Regarding components H_{01} and H_{10} in Appendix A, there are always resonant channels that suppress the evolution between ground states, such as $\Omega_c/\sqrt{2}|E_{0DP}^1\rangle\langle 01D| + \text{H.c.}$ and $\Omega_c/\sqrt{2}|E_{D0P}^1\rangle\langle 10D| + \text{H.c.}$, rendering the vdW term H_{vdw} inconsequential to the evolution of the system. In the experiment, the Stark shifts $\Omega_c^2/(\Delta - V_{13}^D) + \Omega_c^2/(\Delta - V_{23}^D) - 2\Omega_c^2/\Delta$ on the Rydberg states $|D\rangle$ and $\Omega_c^2/(\Delta + V_{13}^P) + \Omega_c^2/(\Delta + V_{23}^P) - 2\Omega_c^2/\Delta$ on $|P\rangle$ of the atom **T3** can be removed by employing two additional laser beams.

[1] H.-A. Engel and D. Loss, Fermionic bell-state analyzer for spin qubits, *Science* **309**, 586 (2005).

[2] R. Ionicioiu, A. E. Popescu, W. J. Munro, and T. P. Spiller,

Generalized parity measurements, *Phys. Rev. A* **78**, 052326 (2008).

[3] O.-P. Saira, J. P. Groen, J. Cramer, M. Meretska, G. de Lange,

- and L. DiCarlo, Entanglement genesis by ancilla-based parity measurement in 2d circuit qed, *Phys. Rev. Lett.* **112**, 070502 (2014).
- [4] S. B. van Dam, J. Cramer, T. H. Taminiu, and R. Hanson, Multipartite entanglement generation and contextuality tests using nondestructive three-qubit parity measurements, *Phys. Rev. Lett.* **123**, 050401 (2019).
- [5] F.-Q. Guo, J.-L. Wu, X.-Y. Zhu, Z. Jin, Y. Zeng, S. Zhang, L.-L. Yan, M. Feng, and S.-L. Su, Complete and nondestructive distinguishment of many-body rydberg entanglement via robust geometric quantum operations, *Phys. Rev. A* **102**, 062410 (2020).
- [6] S. J. Devitt, W. J. Munro, and K. Nemoto, Quantum error correction for beginners, *Reports on Progress in Physics* **76**, 076001 (2013).
- [7] W. P. Livingston, M. S. Blok, E. Flurin, J. Dressel, A. N. Jordan, and I. Siddiqi, Experimental demonstration of continuous quantum error correction, *Nature Communications* **13**, 2307 (2022).
- [8] S. Krinner, N. Lacroix, A. Remm, A. Di Paolo, E. Genois, C. Leroux, C. Hellings, S. Lazar, F. Swiadek, J. Herrmann, G. J. Norris, C. K. Andersen, M. Müller, A. Blais, C. Eichler, and A. Wallraff, Realizing repeated quantum error correction in a distance-three surface code, *Nature* **605**, 669 (2022).
- [9] C. Poole, T. M. Graham, M. A. Perlin, M. Otten, and M. Saffman, *Architecture for fast implementation of qldpc codes with optimized rydberg gates* (2024), arXiv:2404.18809 [quant-ph].
- [10] W. Lechner, P. Hauke, and P. Zoller, A quantum annealing architecture with all-to-all connectivity from local interactions, *Science Advances* **1**, e1500838 (2015).
- [11] C. Dlaska, K. Ender, G. B. Mbeng, A. Kruckenhauser, W. Lechner, and R. van Bijnen, Quantum optimization via four-body rydberg gates, *Phys. Rev. Lett.* **128**, 120503 (2022).
- [12] M. Fellner, A. Messinger, K. Ender, and W. Lechner, Universal parity quantum computing, *Phys. Rev. Lett.* **129**, 180503 (2022).
- [13] K. Ender, R. ter Hoeven, B. E. Niehoff, M. Drieb-Schön, and W. Lechner, Parity Quantum Optimization: Compiler, *Quantum* **7**, 950 (2023).
- [14] M. Takita, A. D. Córcoles, E. Magesan, B. Abdo, M. Brink, A. Cross, J. M. Chow, and J. M. Gambetta, Demonstration of weight-four parity measurements in the surface code architecture, *Phys. Rev. Lett.* **117**, 210505 (2016).
- [15] C. C. Bultink, T. E. O'Brien, R. Vollmer, N. Muthusubramanian, M. W. Beekman, M. A. Rol, X. Fu, B. Tarasinski, V. Ostroukh, B. Varbanov, A. Bruno, and L. DiCarlo, Protecting quantum entanglement from leakage and qubit errors via repetitive parity measurements, *Science Advances* **6**, eaay3050 (2020).
- [16] Google Quantum AI, Suppressing quantum errors by scaling a surface code logical qubit, *Nature* **614**, 676 (2023).
- [17] B. Royer, S. Puri, and A. Blais, Qubit parity measurement by parametric driving in circuit qed, *Science Advances* **4**, eaau1695 (2018).
- [18] S.-L. Su, F.-Q. Guo, L. Tian, X.-Y. Zhu, L.-L. Yan, E.-J. Liang, and M. Feng, Nondestructive rydberg parity meter and its applications, *Phys. Rev. A* **101**, 012347 (2020).
- [19] R.-H. Zheng, Y.-H. Kang, S.-L. Su, J. Song, and Y. Xia, Robust and high-fidelity nondestructive rydberg parity meter, *Phys. Rev. A* **102**, 012609 (2020).
- [20] M. J. Reagor, T. C. Bohdanowicz, D. R. Perez, E. A. Sete, and W. J. Zeng, *Hardware optimized parity check gates for superconducting surface codes* (2022), arXiv:2211.06382 [quant-ph].
- [21] K. S. Christensen, N. T. Zinner, and M. Kjaergaard, Scheme for parity-controlled multi-qubit gates with superconducting qubits (2023), arXiv:2302.00719 [quant-ph].
- [22] T. Itoko, M. Malekakhlagh, N. Kanazawa, and M. Takita, Three-qubit parity gate via simultaneous cross-resonance drives, *Phys. Rev. Appl.* **21**, 034018 (2024).
- [23] M. A. Nielsen and I. Chuang, Quantum computation and quantum information, *Am J Phys* **70**, 558 (2002).
- [24] B. M. Terhal, Quantum error correction for quantum memories, *Rev. Mod. Phys.* **87**, 307 (2015).
- [25] J. Roffe, Quantum error correction: an introductory guide, *Contemp Phys* **60**, 226 (2019).
- [26] P. W. Shor, Scheme for reducing decoherence in quantum computer memory, *Phys. Rev. A* **52**, R2493 (1995).
- [27] A. G. Fowler, M. Mariantoni, J. M. Martinis, and A. N. Cleland, Surface codes: Towards practical large-scale quantum computation, *Phys. Rev. A* **86**, 032324 (2012).
- [28] C. Horsman, A. G. Fowler, S. Devitt, and R. V. Meter, Surface code quantum computing by lattice surgery, *New J. Phys.* **14**, 123011 (2012).
- [29] C. K. Andersen, A. Remm, S. Lazar, S. Krinner, N. Lacroix, G. J. Norris, M. Gabureac, C. Eichler, and A. Wallraff, Repeated quantum error detection in a surface code, *Nat. Phys.* **16**, 875 (2020).
- [30] J. M. Gertler, B. Baker, J. Li, S. Shirol, J. Koch, and C. Wang, Protecting a bosonic qubit with autonomous quantum error correction, *Nature* **590**, 243 (2021).
- [31] D. Gottesman, *Stabilizer codes and quantum error correction*. Caltech Ph. D, Ph.D. thesis, Thesis, eprint: quant-ph/9705052 (1997).
- [32] M. Saffman, T. G. Walker, and K. Mølmer, Quantum information with rydberg atoms, *Rev. Mod. Phys.* **82**, 2313 (2010).
- [33] M. Saffman, Quantum computing with atomic qubits and rydberg interactions: progress and challenges, *Journal of Physics B: Atomic, Molecular and Optical Physics* **49**, 202001 (2016).
- [34] D. Barredo, S. de Léséleuc, V. Lienhard, T. Lahaye, and A. Browaeys, An atom-by-atom assembler of defect-free arbitrary two-dimensional atomic arrays, *Science* **354**, 1021 (2016).
- [35] H. Bernien, S. Schwartz, A. Keesling, H. Levine, A. Omran, H. Pichler, S. Choi, A. S. Zibrov, M. Endres, M. Greiner, V. Vuletić, and M. D. Lukin, Probing many-body dynamics on a 51-atom quantum simulator, *Nature* **551**, 579 (2017).
- [36] X. Wu, X. Liang, Y. Tian, F. Yang, C. Chen, Y.-C. Liu, M. K. Tey, and L. You, A concise review of rydberg atom based quantum computation and quantum simulation*, *Chinese Physics B* **30**, 020305 (2021).
- [37] X.-F. Shi, Quantum logic and entanglement by neutral rydberg atoms: methods and fidelity, *Quantum Science and Technology* **7**, 023002 (2022).
- [38] X.-Q. Shao, S.-L. Su, L. Li, R. Nath, J.-H. Wu, and W. Li, Rydberg superatoms: An artificial quantum system for quantum information processing and quantum optics, *Applied Physics Reviews* **11**, 031320 (2024).
- [39] L. Isenhower, E. Urban, X. L. Zhang, A. T. Gill, T. Henage, T. A. Johnson, T. G. Walker, and M. Saffman, Demonstration of a neutral atom controlled-not quantum gate, *Phys. Rev. Lett.* **104**, 010503 (2010).
- [40] H. Levine, A. Keesling, G. Semeghini, A. Omran, T. T. Wang, S. Ebadi, H. Bernien, M. Greiner, V. Vuletić, H. Pichler, and M. D. Lukin, Parallel implementation of high-fidelity multi-qubit gates with neutral atoms, *Phys. Rev. Lett.* **123**, 170503 (2019).

- [41] X.-Q. Shao, Selective rydberg pumping via strong dipole blockade, *Phys. Rev. A* **102**, 053118 (2020).
- [42] B.-J. Liu, S.-L. Su, and M.-H. Yung, Nonadiabatic noncyclic geometric quantum computation in rydberg atoms, *Phys. Rev. Res.* **2**, 043130 (2020).
- [43] J.-L. Wu, Y. Wang, J.-X. Han, Y.-K. Feng, S.-L. Su, Y. Xia, Y. Jiang, and J. Song, One-step implementation of rydberg-antiblockade swap and controlled-swap gates with modified robustness, *Photon. Res.* **9**, 814 (2021).
- [44] K. McDonnell, L. F. Keary, and J. D. Pritchard, Demonstration of a quantum gate using electromagnetically induced transparency, *Phys. Rev. Lett.* **129**, 200501 (2022).
- [45] S. Ma, A. P. Burgers, G. Liu, J. Wilson, B. Zhang, and J. D. Thompson, Universal gate operations on nuclear spin qubits in an optical tweezer array of ^{171}Yb atoms, *Phys. Rev. X* **12**, 021028 (2022).
- [46] Z. Fu, P. Xu, Y. Sun, Y.-Y. Liu, X.-D. He, X. Li, M. Liu, R.-B. Li, J. Wang, L. Liu, and M.-S. Zhan, High-fidelity entanglement of neutral atoms via a rydberg-mediated single-modulated-pulse controlled-phase gate, *Phys. Rev. A* **105**, 042430 (2022).
- [47] X. X. Li, X. Q. Shao, and W. Li, Single temporal-pulse-modulated parameterized controlled-phase gate for rydberg atoms, *Phys. Rev. Appl.* **18**, 044042 (2022).
- [48] S. Jandura, J. D. Thompson, and G. Pupillo, Optimizing rydberg gates for logical-qubit performance, *PRX Quantum* **4**, 020336 (2023).
- [49] S. J. Evered, D. Bluvstein, M. Kalinowski, S. Ebadi, T. Manovitz, H. Zhou, S. H. Li, A. A. Geim, T. T. Wang, N. Maskara, H. Levine, G. Semeghini, M. Greiner, V. Vuletić, and M. D. Lukin, High-fidelity parallel entangling gates on a neutral-atom quantum computer, *Nature* **622**, 268 (2023).
- [50] S. Ma, G. Liu, P. Peng, B. Zhang, S. Jandura, J. Claes, A. P. Burgers, G. Pupillo, S. Puri, and J. D. Thompson, High-fidelity gates and mid-circuit erasure conversion in an atomic qubit, *Nature* **622**, 279 (2023).
- [51] N. Heimann, L. Broers, N. Pintul, T. Petersen, K. Sponselee, A. Ilin, C. Becker, and L. Mathey, Quantum gate optimization for rydberg architectures in the weak-coupling limit (2023), [arXiv:2306.08691 \[quant-ph\]](https://arxiv.org/abs/2306.08691).
- [52] M. Saffman and K. Mølmer, Efficient multiparticle entanglement via asymmetric rydberg blockade, *Phys. Rev. Lett.* **102**, 240502 (2009).
- [53] T. Wilk, A. Gaëtan, C. Evellin, J. Wolters, Y. Miroshnychenko, P. Grangier, and A. Browaeys, Entanglement of two individual neutral atoms using rydberg blockade, *Phys. Rev. Lett.* **104**, 010502 (2010).
- [54] Y.-Y. Jau, A. M. Hankin, T. Keating, I. H. Deutsch, and G. W. Biedermann, Entangling atomic spins with a rydberg-dressed spin-flip blockade, *Nat. Phys.* **12**, 71 (2016).
- [55] H. Levine, A. Keesling, A. Omran, H. Bernien, S. Schwartz, A. S. Zibrov, M. Endres, M. Greiner, V. Vuletić, and M. D. Lukin, High-fidelity control and entanglement of rydberg-atom qubits, *Phys. Rev. Lett.* **121**, 123603 (2018).
- [56] T. M. Graham, M. Kwon, B. Grinkemeyer, Z. Marra, X. Jiang, M. T. Lichtman, Y. Sun, M. Ebert, and M. Saffman, Rydberg-mediated entanglement in a two-dimensional neutral atom qubit array, *Phys. Rev. Lett.* **123**, 230501 (2019).
- [57] I. S. Madjarov, J. P. Covey, A. L. Shaw, J. Choi, A. Kale, A. Cooper, H. Pichler, V. Schkolnik, J. R. Williams, and M. Endres, High-fidelity entanglement and detection of alkaline-earth rydberg atoms, *Nat. Phys.* **16**, 857 (2020).
- [58] S. Hollerith, K. Srakaew, D. Wei, A. Rubio-Abadal, D. Adler, P. Weckesser, A. Kruckenhauser, V. Walther, R. van Bijnen, J. Rui, C. Gross, I. Bloch, and J. Zeiher, Realizing distance-selective interactions in a rydberg-dressed atom array, *Phys. Rev. Lett.* **128**, 113602 (2022).
- [59] G.-S. Ye, B. Xu, Y. Chang, S. Shi, T. Shi, and L. Li, A photonic entanglement filter with rydberg atoms, *Nat. Photonics* **17**, 538 (2023).
- [60] A. L. Shaw, Z. Chen, J. Choi, D. K. Mark, P. Scholl, R. Finkelstein, A. Elben, S. Choi, and M. Endres, Benchmarking highly entangled states on a 60-atom analogue quantum simulator, *Nature* **628**, 71 (2024).
- [61] S. de Léséleuc, V. Lienhard, P. Scholl, D. Barredo, S. Weber, N. Lang, H. P. Büchler, T. Lahaye, and A. Browaeys, Observation of a symmetry-protected topological phase of interacting bosons with rydberg atoms, *Science* **365**, 775 (2019).
- [62] A. Browaeys and T. Lahaye, Many-body physics with individually controlled rydberg atoms, *Nat. Phys.* **16**, 132 (2020).
- [63] V. Lienhard, P. Scholl, S. Weber, D. Barredo, S. de Léséleuc, R. Bai, N. Lang, M. Fleischhauer, H. P. Büchler, T. Lahaye, and A. Browaeys, Realization of a density-dependent peierls phase in a synthetic, spin-orbit coupled rydberg system, *Phys. Rev. X* **10**, 021031 (2020).
- [64] X. Wu, F. Yang, S. Yang, K. Mølmer, T. Pohl, M. K. Tey, and L. You, Manipulating synthetic gauge fluxes via multicolor dressing of rydberg-atom arrays, *Phys. Rev. Res.* **4**, L032046 (2022).
- [65] X. X. Li, J. B. You, X. Q. Shao, and W. Li, Coherent ground-state transport of neutral atoms, *Phys. Rev. A* **105**, 032417 (2022).
- [66] L. Su, A. Douglas, M. Szurek, R. Groth, S. F. Ozturk, A. Krahn, A. H. Hébert, G. A. Phelps, S. Ebadi, S. Dickerson, F. Ferlaino, O. Marković, and M. Greiner, Dipolar quantum solids emerging in a hubbard quantum simulator, *Nature* **622**, 724 (2023).
- [67] D. Malz and J. I. Cirac, Few-body analog quantum simulation with rydberg-dressed atoms in optical lattices, *PRX Quantum* **4**, 020301 (2023).
- [68] M. Kalinowski, N. Maskara, and M. D. Lukin, Non-abelian floquet spin liquids in a digital rydberg simulator, *Phys. Rev. X* **13**, 031008 (2023).
- [69] M. C. Tran, D. K. Mark, W. W. Ho, and S. Choi, Measuring arbitrary physical properties in analog quantum simulation, *Phys. Rev. X* **13**, 011049 (2023).
- [70] Z. Yan, Y.-C. Wang, R. Samajdar, S. Sachdev, and Z. Y. Meng, Emergent glassy behavior in a kagome rydberg atom array, *Phys. Rev. Lett.* **130**, 206501 (2023).
- [71] Z. Zeybek, R. Mukherjee, and P. Schmelcher, Quantum phases from competing van der waals and dipole-dipole interactions of rydberg atoms, *Phys. Rev. Lett.* **131**, 203003 (2023).
- [72] K. Kim, F. Yang, K. Mølmer, and J. Ahn, Realization of an extremely anisotropic heisenberg magnet in rydberg atom arrays, *Phys. Rev. X* **14**, 011025 (2024).
- [73] D. Jaksch, J. I. Cirac, P. Zoller, S. L. Rolston, R. Côté, and M. D. Lukin, Fast quantum gates for neutral atoms, *Phys. Rev. Lett.* **85**, 2208 (2000).
- [74] M. D. Lukin, M. Fleischhauer, R. Cote, L. M. Duan, D. Jaksch, J. I. Cirac, and P. Zoller, Dipole blockade and quantum information processing in mesoscopic atomic ensembles, *Phys. Rev. Lett.* **87**, 037901 (2001).
- [75] C. Ates, T. Pohl, T. Pattard, and J. M. Rost, Antiblockade in rydberg excitation of an ultracold lattice gas, *Phys. Rev. Lett.* **98**, 023002 (2007).
- [76] J. E. Johnson and S. L. Rolston, Interactions between rydberg-dressed atoms, *Phys. Rev. A* **82**, 033412 (2010).
- [77] N. Henkel, R. Nath, and T. Pohl, Three-dimensional roton

- excitations and supersolid formation in rydberg-excited bose-einstein condensates, *Phys. Rev. Lett.* **104**, 195302 (2010).
- [78] Y. Wang, S. Shevate, T. M. Wintermantel, M. Morgado, G. Lochead, and S. Whitlock, Preparation of hundreds of microscopic atomic ensembles in optical tweezer arrays, *NPJ Quantum Inf.* **6**, 54 (2020).
- [79] S. Ebadi, T. T. Wang, H. Levine, A. Keesling, G. Semeghini, A. Omran, D. Bluvstein, R. Samajdar, H. Pichler, W. W. Ho, S. Choi, S. Sachdev, M. Greiner, V. Vuletić, and M. D. Lukin, Quantum phases of matter on a 256-atom programmable quantum simulator, *Nature* **595**, 227 (2021).
- [80] P. Scholl, M. Schuler, H. J. Williams, A. A. Eberharter, D. Barredo, K.-N. Schymik, V. Lienhard, L.-P. Henry, T. C. Lang, T. Lahaye, A. M. Läuchli, and A. Browaeys, Quantum simulation of 2d antiferromagnets with hundreds of rydberg atoms, *Nature* **595**, 233 (2021).
- [81] T. M. Graham, Y. Song, J. Scott, C. Poole, L. Phuttitarn, K. Jooya, P. Eichler, X. Jiang, A. Marra, B. Grinkemeyer, M. Kwon, M. Ebert, J. Cherek, M. T. Lichtman, M. Gillette, J. Gilbert, D. Bowman, T. Ballance, C. Campbell, E. D. Dahl, O. Crawford, N. S. Blunt, B. Rogers, T. Noel, and M. Saffman, Multi-qubit entanglement and algorithms on a neutral-atom quantum computer, *Nature* **604**, 457 (2022).
- [82] D. Crow, R. Joynt, and M. Saffman, Improved error thresholds for measurement-free error correction, *Phys. Rev. Lett.* **117**, 130503 (2016).
- [83] J. M. Auger, S. Bergamini, and D. E. Browne, Blueprint for fault-tolerant quantum computation with rydberg atoms, *Phys. Rev. A* **96**, 052320 (2017).
- [84] I. Cong, H. Levine, A. Keesling, D. Bluvstein, S.-T. Wang, and M. D. Lukin, Hardware-efficient, fault-tolerant quantum computation with rydberg atoms, *Phys. Rev. X* **12**, 021049 (2022).
- [85] Y. Wu, S. Kolkowitz, S. Puri, and J. D. Thompson, Erasure conversion for fault-tolerant quantum computing in alkaline earth rydberg atom arrays, *Nat. Commun.* **13**, 4657 (2022).
- [86] P. Scholl, A. L. Shaw, R. B.-S. Tsai, R. Finkelstein, J. Choi, and M. Endres, Erasure conversion in a high-fidelity rydberg quantum simulator, *Nature* **622**, 273 (2023).
- [87] M. A. Perlin, V. N. Premakumar, J. Wang, M. Saffman, and R. Joynt, Fault-tolerant measurement-free quantum error correction with multiqubit gates, *Phys. Rev. A* **108**, 062426 (2023).
- [88] M. Kang, W. C. Campbell, and K. R. Brown, Quantum error correction with metastable states of trapped ions using erasure conversion, *PRX Quantum* **4**, 020358 (2023).
- [89] D. Bluvstein, S. J. Evered, A. A. Geim, S. H. Li, H. Zhou, T. Manovitz, S. Ebadi, M. Cain, M. Kalinowski, D. Hangleiter, J. P. Bonilla Ataides, N. Maskara, I. Cong, X. Gao, P. Sales Rodriguez, T. Karolyshyn, G. Semeghini, M. J. Gullans, M. Greiner, V. Vuletić, and M. D. Lukin, Logical quantum processor based on reconfigurable atom arrays, *Nature* **626**, 58 (2024).
- [90] S. Heußen, D. F. Locher, and M. Müller, Measurement-free fault-tolerant quantum error correction in near-term devices, *PRX Quantum* **5**, 010333 (2024).
- [91] L. Pecorari, S. Jandura, G. K. Brennen, and G. Pupillo, High-rate quantum ldpc codes for long-range-connected neutral atom registers (2024), arXiv:2404.13010 [quant-ph].
- [92] S. Jandura and G. Pupillo, Surface code stabilizer measurements for rydberg atoms (2024), arXiv:2405.16621 [quant-ph].
- [93] D. X. Li and X. Q. Shao, Unconventional rydberg pumping and applications in quantum information processing, *Phys. Rev. A* **98**, 062338 (2018).
- [94] X. Q. Shao, F. Liu, X. W. Xue, W. L. Mu, and W. Li, High-fidelity interconversion between greenberger-horne-zeilinger and w states through floquet-lindblad engineering in rydberg atom arrays, *Phys. Rev. Appl.* **20**, 014014 (2023).
- [95] Y. Zhao, Y.-Q. Yang, W. Li, and X.-Q. Shao, Dissipative stabilization of high-dimensional GHZ states for neutral atoms, *Applied Physics Letters* **124**, 114001 (2024).
- [96] G. F. Xu, J. Zhang, D. M. Tong, E. Sjöqvist, and L. C. Kwek, Nonadiabatic holonomic quantum computation in decoherence-free subspaces, *Phys. Rev. Lett.* **109**, 170501 (2012).
- [97] E. Sjöqvist, D. M. Tong, L. M. Andersson, B. Hessmo, M. Johansson, and K. Singh, Non-adiabatic holonomic quantum computation, *New J. Phys.* **14**, 103035 (2012).
- [98] J. Zhang, T. H. Kyaw, S. Filipp, L.-C. Kwek, E. Sjöqvist, and D. Tong, Geometric and holonomic quantum computation, *Physics Reports* **1027**, 1 (2023), geometric and holonomic quantum computation.
- [99] Y. Liang, P. Shen, T. Chen, and Z.-Y. Xue, Nonadiabatic holonomic quantum computation and its optimal control, *Science China Information Sciences* **66**, 180502 (2023).
- [100] P.-Y. Song, J.-F. Wei, P. Xu, L.-L. Yan, M. Feng, S.-L. Su, and G. Chen, Fast realization of high-fidelity nonadiabatic holonomic quantum gates with a time-optimal-control technique in rydberg atoms, *Phys. Rev. A* **109**, 022613 (2024).
- [101] D. Barredo, H. Labuhn, S. Ravets, T. Lahaye, A. Browaeys, and C. S. Adams, Coherent excitation transfer in a spin chain of three rydberg atoms, *Phys. Rev. Lett.* **114**, 113002 (2015).
- [102] S. de Léséleuc, D. Barredo, V. Lienhard, A. Browaeys, and T. Lahaye, Optical control of the resonant dipole-dipole interaction between rydberg atoms, *Phys. Rev. Lett.* **119**, 053202 (2017).
- [103] Z.-P. Hong, B.-J. Liu, J.-Q. Cai, X.-D. Zhang, Y. Hu, Z. D. Wang, and Z.-Y. Xue, Implementing universal nonadiabatic holonomic quantum gates with transmons, *Phys. Rev. A* **97**, 022332 (2018).
- [104] Y. Xu, W. Cai, Y. Ma, X. Mu, L. Hu, T. Chen, H. Wang, Y. P. Song, Z.-Y. Xue, Z.-q. Yin, and L. Sun, Single-loop realization of arbitrary nonadiabatic holonomic single-qubit quantum gates in a superconducting circuit, *Phys. Rev. Lett.* **121**, 110501 (2018).
- [105] Y. Liu, Y. Sun, Z. Fu, P. Xu, X. Wang, X. He, J. Wang, and M. Zhan, Infidelity induced by ground-rydberg decoherence of the control qubit in a two-qubit rydberg-blockade gate, *Phys. Rev. Appl.* **15**, 054020 (2021).
- [106] D. Tong, S. M. Farooqi, J. Stanojevic, S. Krishnan, Y. P. Zhang, R. Côté, E. E. Eyler, and P. L. Gould, Local blockade of rydberg excitation in an ultracold gas, *Phys. Rev. Lett.* **93**, 063001 (2004).
- [107] P. Thoumany, T. Hänsch, G. Stania, L. Urbonas, and T. Becker, Optical spectroscopy of rubidium rydberg atoms with a 297 nm frequency-doubled dye laser, *Opt. Lett.* **34**, 1621 (2009).
- [108] S. Wüster, C. Ates, A. Eisfeld, and J. M. Rost, Excitation transport through rydberg dressing, *New Journal of Physics* **13**, 073044 (2011).
- [109] A. W. Glaetzle, R. M. W. van Bijnen, P. Zoller, and W. Lechner, A coherent quantum annealer with rydberg atoms, *Nature Communications* **8**, 15813 (2017).
- [110] B. Li, M. Li, X. Jiang, J. Qian, X. Li, L. Liu, and Y. Wang, Optical spectroscopy of np rydberg states of ^{87}Rb atoms with a 297-nm ultraviolet laser, *Phys. Rev. A* **99**, 042502 (2019).
- [111] K. Srakaew, P. Weckesser, S. Hollerith, D. Wei, D. Adler, I. Bloch, and J. Zeiher, A subwavelength atomic array switched by a single rydberg atom, *Nat. Phys.* **19**, 714 (2023).

- [112] I. I. Ryabtsev, I. I. Beterov, D. B. Tretyakov, V. M. Entin, and E. A. Yakshina, Doppler- and recoil-free laser excitation of rydberg states via three-photon transitions, *Phys. Rev. A* **84**, 053409 (2011).
- [113] I. I. Beterov, I. N. Ashkarin, E. A. Yakshina, D. B. Tretyakov, V. M. Entin, I. I. Ryabtsev, P. Cheinet, P. Pillet, and M. Saffman, Fast three-qubit toffoli quantum gate based on three-body förster resonances in rydberg atoms, *Phys. Rev. A* **98**, 042704 (2018).
- [114] P. Cheinet, K.-L. Pham, P. Pillet, I. Beterov, I. Ashkarin, D. Tretyakov, E. Yakshina, V. Entin, and I. Ryabtsev, Three-body förster resonance of a new type in rydberg atoms, *Quantum Electronics* **50**, 213 (2020).
- [115] I. N. Ashkarin, I. I. Beterov, E. A. Yakshina, D. B. Tretyakov, V. M. Entin, I. I. Ryabtsev, P. Cheinet, K.-L. Pham, S. Lepoutre, and P. Pillet, Toffoli gate based on a three-body fine-structure-state-changing förster resonance in rydberg atoms, *Phys. Rev. A* **106**, 032601 (2022).
- [116] D. B. Tretyakov, V. M. Entin, I. I. Beterov, E. A. Yakshina, Y. Y. Pechersky, V. G. Gol'dort, and I. I. Ryabtsev, Two-photon laser excitation of rb rydberg atoms in the magneto-optical trap and vapor cell, *Photonics* **10**, 10.3390/photonics10111201 (2023).
- [117] M. Saffman, I. I. Beterov, A. Dalal, E. J. Pérez, and B. C. Sanders, Symmetric rydberg controlled- z gates with adiabatic pulses, *Phys. Rev. A* **101**, 062309 (2020).
- [118] J. F. Haase, Z.-Y. Wang, J. Casanova, and M. B. Plenio, Soft quantum control for highly selective interactions among joint quantum systems, *Phys. Rev. Lett.* **121**, 050402 (2018).
- [119] X.-F. Shi and T. A. B. Kennedy, Annulled van der waals interaction and fast rydberg quantum gates, *Phys. Rev. A* **95**, 043429 (2017).
- [120] E. Urban, T. A. Johnson, T. Henage, L. Isenhower, D. D. Yavuz, T. G. Walker, and M. Saffman, Observation of rydberg blockade between two atoms, *Nature Physics* **5**, 110 (2009).
- [121] E. Robertson, N. Šibalić, R. Potvliege, and M. Jones, Arc 3.0: An expanded python toolbox for atomic physics calculations, *Comput Phys Commun* **261**, 107814 (2021).
- [122] X.-F. Shi and Y. Lu, Quantum gates with weak van der waals interactions of neutral rydberg atoms, *Phys. Rev. A* **104**, 012615 (2021).
- [123] Y. Chew, T. Tomita, T. P. Mahesh, S. Sugawa, S. de Léséleuc, and K. Ohmori, Ultrafast energy exchange between two single rydberg atoms on a nanosecond timescale, *Nature Photonics* **16**, 724 (2022).
- [124] N. Lorenz, L. Festa, L.-M. Steinert, and C. Gross, Raman sideband cooling in optical tweezer arrays for Rydberg dressing, *SciPost Phys.* **10**, 052 (2021).
- [125] H. Hwang, A. Byun, and J. Ahn, Eit cooling of atoms in optical dipole traps, in *2021 Conference on Lasers and Electro-Optics (CLEO)* (2021) pp. 1–2.
- [126] L. Zhao, M. D. K. Lee, M. M. Aliyu, and H. Loh, Floquet-tailored rydberg interactions, *Nat. Commun.* **14**, 7128 (2023).
- [127] S. de Léséleuc, D. Barredo, V. Lienhard, A. Browaeys, and T. Lahaye, Analysis of imperfections in the coherent optical excitation of single atoms to rydberg states, *Phys. Rev. A* **97**, 053803 (2018).
- [128] H. Jo, Y. Song, M. Kim, and J. Ahn, Rydberg atom entanglements in the weak coupling regime, *Phys. Rev. Lett.* **124**, 033603 (2020).
- [129] X. L. Zhang, A. T. Gill, L. Isenhower, T. G. Walker, and M. Saffman, Fidelity of a rydberg-blockade quantum gate from simulated quantum process tomography, *Phys. Rev. A* **85**, 042310 (2012).
- [130] R. Li, J. Qian, and W. Zhang, Proposal for practical rydberg quantum gates using a native two-photon excitation, *Quantum Science and Technology* **8**, 035032 (2023).
- [131] R. B.-S. Tsai, X. Sun, A. L. Shaw, R. Finkelstein, and M. Endres, Benchmarking and fidelity response theory of high-fidelity rydberg entangling gates (2024), arXiv:2407.20184 [quant-ph].
- [132] V. N. Premakumar, H. Sha, D. Crow, E. Bach, and R. Joynt, 2-designs and redundant syndrome extraction for quantum error correction, *Quantum Information Processing* **20**, 84 (2021).
- [133] Google Quantum AI, Exponential suppression of bit or phase errors with cyclic error correction, *Nature* **595**, 383 (2021).
- [134] J. P. Bonilla Ataides, D. K. Tuckett, S. D. Bartlett, S. T. Flammia, and B. J. Brown, The xxxz surface code, *Nat. Commun.* **12**, 2172 (2021).
- [135] J. F. Marques, B. M. Varbanov, M. S. Moreira, H. Ali, N. Muthusubramanian, C. Zachariadis, F. Battistel, M. Beekman, N. Haider, W. Vlothuizen, A. Bruno, B. M. Terhal, and L. DiCarlo, Logical-qubit operations in an error-detecting surface code, *Nat. Phys.* **18**, 80 (2022).
- [136] Y. Zhao, Y. Ye, H.-L. Huang, Y. Zhang, D. Wu, H. Guan, Q. Zhu, Z. Wei, T. He, S. Cao, F. Chen, T.-H. Chung, H. Deng, D. Fan, M. Gong, C. Guo, S. Guo, L. Han, N. Li, S. Li, Y. Li, F. Liang, J. Lin, H. Qian, H. Rong, H. Su, L. Sun, S. Wang, Y. Wu, Y. Xu, C. Ying, J. Yu, C. Zha, K. Zhang, Y.-H. Huo, C.-Y. Lu, C.-Z. Peng, X. Zhu, and J.-W. Pan, Realization of an error-correcting surface code with superconducting qubits, *Phys. Rev. Lett.* **129**, 030501 (2022).
- [137] A. Vepsäläinen, S. Danilin, and G. S. Paraoanu, Optimal superadiabatic population transfer and gates by dynamical phase corrections, *Quantum Science and Technology* **3**, 024006 (2018).
- [138] A. Vepsäläinen, S. Danilin, and G. S. Paraoanu, Superadiabatic population transfer in a three-level superconducting circuit, *Sci. Adv.* **5**, eaau5999 (2019).
- [139] S.-L. Su, E. Liang, S. Zhang, J.-J. Wen, L.-L. Sun, Z. Jin, and A.-D. Zhu, One-step implementation of the rydberg-rydberg-interaction gate, *Phys. Rev. A* **93**, 012306 (2016).
- [140] Y. J. Zhao, B. Liu, Y. Q. Ji, S. Q. Tang, and X. Q. Shao, Robust generation of entangled state via ground-state antiblockade of rydberg atoms, *Sci Rep* **7**, 16489 (2017).
- [141] C. Wang, J.-X. Han, J.-L. Wu, Y. Wang, Y. Jiang, Y. Xia, and J. Song, Generation of three-dimensional entanglement between two antiblockade rydberg atoms with detuning-compensation-induced effective resonance, *Laser Phys.* **30**, 045201 (2020).
- [142] J.-X. Han, J.-L. Wu, Y. Wang, Y.-Y. Jiang, Y. Xia, and J. Song, Multi-qubit phase gate on multiple resonators mediated by a superconducting bus, *Opt. Express* **28**, 1954 (2020).